COMMUNICATIONS PHYSICS

ARTICLE

https://doi.org/10.1038/s42005-019-0191-z OPEN

Near-field acoustic manipulation in a confined evanescent Bessel beam

Pierre-Yves Gires [1] & Cédric Poulain[1]

We demonstrate the potential of using evanescent fields, instead of conventional propagating sound fields, to manipulate particles at micro or nano scale. We generate an evanescent acoustic Bessel beam in liquid above a thin, circular, asymmetrically excited plate. In the sub-MHz ultrasound domain, the resulting radiation force causes the particles to assemble at the pressure antinodes along concentric circles corresponding to the Bessel profile. By imposing an axial confinement in the evanescent region, the subwavelength two-plate sandwich system becomes resonant, increasing the radiation force magnitude. Resonances occur for some well-defined gaps for which whole numbers of antinodal circles are observed. Through fine tuning, particles as small as bacteria can be patterned. Further amplification can be obtained by trapping a microbubble in the Bessel beam axis. As we show, this resonant bubble, which acts as an acoustic magnet, can be used to efficiently capture or repel nearby micro-particles.

[1] University Grenoble Alpes, CEA LETI MINATEC Campus, F-38054 Grenoble, France. Correspondence and requests for materials should be addressed to C.P. (email: cedric.poulain@neel.cnrs.fr)

Momentum transfer from radiative electromagnetic and acoustic fields to matter at microscale has been a topic of significant research interest in recent decades. In propagative optics, remarkable applications in trapping microparticles (optical tweezers[1]) and atoms (laser cooling[2]) have been achieved. More recently, manipulation by optical evanescent fields, instead of conventional propagating (i.e. radiative) fields, has become possible thanks to the emergence of nano-photonics and plasmonics[3]. Surface plasmons are electromagnetic and evanescent surface modes confined at a metal-dielectric interface. They can give rise to a plasmon radiation force, which has strong potential for optical sorting[4].

In the meantime, acoustic tweezers have been developed in the radiative acoustic domain, giving birth to a new branch of physics binding acoustics and microfluidics in the field of acoustofluidics[5]. Acoustofluidic chips mainly employ propagative (i.e. radiative) fields mostly based on the use of standing bulk and surface acoustic waves (BAW and SAW, respectively). BAW and SAW (commonly of leaky Rayleigh type) are emitted at high frequency (in the MHz range) to maximize the associated radiation force. Surprisingly, and unlike their electromagnetic counterpart, the use of non-radiative acoustic-based forces has attracted little attention to date. To the best of our knowledge, no prediction of the radiation force in an evanescent acoustic field exists. Likewise, only a few experimental works[6–8] report on manipulation by evanescent acoustic fields. This lack seems paradoxical in view of the main features of evanescent waves. Indeed, regardless of their nature, in a non-radiative field, waves can be confined to an ultra-small region of sub-wavelength dimensions and break the diffraction limit. Besides, their intrinsic in-plane near-field confinement is a key feature of contactless lab-on-a-chip applications.

Furthermore, Durnin[9] was the first to propose Bessel beams in optics as a diffraction-free beam solution of the Helmholtz equation. Bessel beams propagate in free space without undergoing diffraction and retain their transverse pattern as a result. Since then, the optical Bessel field has been the subject of intensive research leading to today's evanescent versions of the Bessel beam (see[10] and references therein). In acoustics, the potency of propagative Bessel beams has recently been demonstrated in the creation of acoustic tweezers using arrays of ultrasonic transducers[11–13], but no evanescent version has been reported so far.

Here, we report on a simple strategy to create an acoustic evanescent Bessel beam for acoustofluidic applications, that only requires a single piezoelectric element. Our present approach stems from[8], where evanescent waves are favored through the excitation of an ultra-thin circular substrate. At a low frequency, the flexural plate waves are subsonic interfacial guided waves similar to plasmon waves in the electromagnetic domain. In this way, we generate an evanescent Bessel beam of order zero in the liquid above the plate. The beam is firstly analyzed in infinite liquid conditions prior to studying the effect of confinement. As we show, when the Bessel beam is confined to evanescence length, resonances occur in the system and its trapping capabilities are enhanced. Lastly, we demonstrate how this beam can excite a trapped single sub-wavelength resonant bubble thanks to the low-frequency regime. The microbubble enhancement then competes with the near-field radiation force due to the Bessel beam, enabling either to attract or repel the neighboring particles.

Results

Evanescent acoustic Bessel beam emission. All the devices used in the present study are made of a circular thin glass plate fixed by a double sided tape onto an annular piezoceramic. The ceramic is a ring of 8.5 mm internal radius covered by a 150-µm-thick glass plate. In the first part of this study, a polypropylene cylinder (15 mm inner radius) is used to contain the liquid above the plate. The cylinder is simply taped onto the piezoceramic and filled up with water up to $h_l = 20$ mm (see Fig. 1a). The ceramic is excited at resonance ($f = 45\ kHz$) by a signal generator and an amplifier. The resonant frequency is determined by the electromechanical analysis (electric impedance measurement) of the whole system (see Supplementary Fig. 1 and Methods).

The acoustic pressure amplitude $P(r,z)$ is measured with a needle hydrophone (see Methods) mounted on a 3-axes translation stages setup. The radial dependence for several heights, from 100 µm to 2 mm, is presented in Fig. 1b. All measurements are made with a voltage of 20 V_{pp}, where the

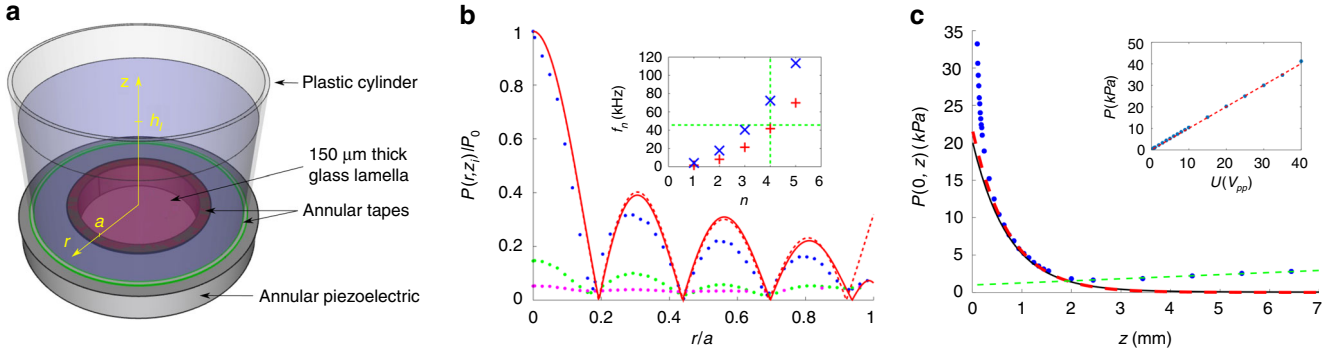

Fig. 1 Evanescent acoustic Bessel beam characterization. **a** Unconfined device and notations. The tape internal radius is $a = 9$ mm. **b** Normalized acoustic pressure as a function of the radial distance for $z \in \{0.1; 1.1; 2.1\}$ mm in blue, green and pink, respectively. Voltage $U = 20\ V_{pp}$, $f = 45\ kHz$. P is normalized by $P_0 = P(r = 0,\ z = 0.1\,\text{mm}) = 34$ kPa. Solid red line: calculated pressure P assuming a free boundary plate (using Rayleigh integral). Dotted red line: comparison with the full Bessel shape $J_0\left(\lambda_{04}\frac{r}{a}\right) + C_{04}I_0\left(\lambda_{04}\frac{r}{a}\right)$, having $\lambda_{04} = 12.51$ and $C_{04} = 5.10^{-6}$. Insert: eigenfrequencies of the system (from Eq. 3). Blue: unloaded. Red: infinitely loaded. Dashed green lines correspond to the experimental realization. **c** Evanescent pressure field for $U = 20\ V_{pp}$. Blue: measures. Solid black line: calculated pressure for a plate amplitude of 0.1 µm. This amplitude is chosen for its best fit with the measured pressure at 1 mm. The higher measured pressures for heights smaller than the sensor radius (750 µm) are assumed to be affected by near field effects between the plate and the sensor membrane. Dashed red: theoretical pressure approached neglecting boundary effects, with $P = P(r = 0, z = 0)e^{-k_z z}$ and $k_z = \sqrt{k_r^2 - k_l^2}$ ($1/k_z = 0.7$ mm). Dashed green: linear fit for $z \geq 4$ mm. Insert: Pressure amplitude $P(r = 0,\ z = 0.2\ \text{mm})$ as function of the voltage U. Blue: measures. Dashed red: linear fit, with $P(\text{kPa}) = \alpha U(V_{pp})$ and $\alpha = 1\ \text{kPa}.V_{pp}^{-1}$

electroacoustic emission is in the linear regime (see insert Fig. 1c). The radial evolution presents an invariant structure, characteristic of a non diffracting beam, with four pressure nodes of constant position. The whole pattern vanishes exponentially with the distance normal to the plate, as shown on Fig. 1c (on the beam axis). An exponential fit yields to an evanescent decay length of $1/k_z = 800$ µm, much smaller than the acoustic wavelength in the liquid ($\lambda_l = 33$ mm).

For a solid plate of thickness h_s and density ρ_s loaded by a liquid of density ρ_l, the plate vertical deflection w obeys a wave equation given by:

$$\rho_s h_s \frac{\partial^2 w}{\partial t^2} + D\nabla^4 w = -p(r,0), \quad (1)$$

where $D = \frac{Eh_s^3}{12(1-\nu^2)}$ is the flexural modulus, with E and ν the substrate Young modulus and Poisson ratio, respectively (Supplementary Table 1)[14].

The plate vibration is coupled to the normal stress in the liquid by the pressure term at the right hand side: p, which must satisfy the Helmholtz equation $\Delta p + k_l^2 p = 0$, where $k_l = \omega/c_l$ and c_l the speed of sound in the liquid.

In this system, the effect of loading is classically estimated by assuming that the liquid does not alter the eigenmodes shape but only their frequency[14]. Thus, the nth axisymmetric flexural mode has a deflection $W_n(r)\cos(\omega t)$ following

$$W_n(r)/W_n(0) = J_0(\lambda_{0n} r/a) + C_{0n} I_0(\lambda_{0n} r/a), \quad (2)$$

where J_0 and I_0 are the ordinary and first order modified Bessel functions of order 0, respectively. The $\{\lambda_{0n}, C_{0n}\}$ are determined by the boundary conditions at the plate edge[14]. As a result of the liquid load, the eigenfrequencies become smaller as follows

$$f_n^{\text{load}} = \frac{f_n^{\text{unload}}}{\sqrt{1 + \Gamma_{0n}\frac{\rho_l a}{\rho_s h_s}}}, \quad (3)$$

where $f_n^{\text{unload}} = \frac{1}{2\pi}\frac{\lambda_{0n}^2}{a^2}\left(\frac{D}{\rho_s h_s}\right)^{\frac{1}{2}}$ is the n mode unloaded eigenfrequency, with the non dimensional added mass factor Γ_{0n} that also depends on the plate boundary conditions[14].

In the absence of loading, the corresponding plate phase velocity is $c_s = \left(\frac{D\omega^2}{\rho_s h_s}\right)^{1/4} \propto \sqrt{h_s \omega}$, with ω the driving pulsation. The additional liquid alters the dispersion relation and therefore the corresponding phase velocity c_s of plate waves. In both cases, the propagative (radiative) or non-propagative (evanescent) regime of emission is determined by the supersonic or subsonic domain of emission, which is frequency dependent due to the surface waves dispersivity. In particular, for wave modes with $c_s < c_l$, no radiation is possible: the regime is subsonic and the normal wavenumber k_z is imaginary (evanescent regime). Here the use of very thin substrates in conjunction with low-frequency excitation favors subsonic modes interfacial waves as we will now show.

For any location M in the liquid, the emitted field $p = \Re(\boldsymbol{P}(\boldsymbol{M})e^{j\omega t})$ can be calculated by summing up elementary contributions from every point M' of the plate (Rayleigh integral) $\boldsymbol{P}(\boldsymbol{M}) = \frac{\rho_L}{2\pi}\int_{\boldsymbol{M'}\in\text{plate}} \frac{1}{r'}\frac{\partial^2 \boldsymbol{w}(\boldsymbol{M'})}{\partial t^2} e^{-jk_l r'} dS(\boldsymbol{M'})$ with $r' = ||\boldsymbol{MM'}||$[15].

This calculation for our thin plate excited at $f = 45\,kHz$ assuming free edge conditions yields to the solid lines in Fig. 1b (red) and c (black), in good agreement with experimental data. Note that as in Eq. 2 the I_0 term is negligible away from the borders, the membrane shape can be approached by a Bessel shape, known to be the radial contribution of a cylindrical eigenfunction of the Helmholtz equation[9,16]. As for the normal evanescent profile, the small deviations observed very close to the plate and further than 2 mm are likely to be caused by the sensor perturbation and by the background propagative field emitted by the cylindrical container, respectively. Finally, the insert Fig. 1b confirms the measured $n = 4$ expected for the working frequency ($f = 45\,kHz$) for a free-edge plate (calculated from Eq. (3), see also Supplementary Fig. 2 and Supplementary Table 2).

Therefore, we conclude that the pressure field in the vicinity of the plate at resonance is well approximated by a $n = 4$ evanescent Bessel beam

$$p_1 = P_0 J_0(k_r r) e^{-k_z z}\cos(\omega t), \quad (4)$$

where $k_r = \lambda_{04}/a$ and $k_z = \sqrt{k_r^2 - k_l^2}$. As $k_r \gg k_l$, the loaded plate wave velocity simplifies to $c_s = \frac{\omega}{k_x} = \left(\frac{D\omega^3}{\rho_l}\right)^{\frac{1}{5}} = 213\,\text{m s}^{-1} \ll c_l = 1500\,\text{m s}^{-1}$, confirming the subsonic domain of emission.

Pattern formation. The water is now seeded with polystyrene microparticles (10 and 100 µm) in order to study the behavior of subwavelength particles in the Bessel beam. In the previous setup (infinite liquid condition), no pattern was observed within reasonable times (a few minutes). When the liquid height is reduced down to $h_l = 1$ mm, the acoustic pressure is increased by a factor 2.3 so that a visible pattern starts to form. Note that for small heights ($h_l \le 1$ mm), the water can sustain its own weight by capillarity, so that the confining cylinder can be removed, as shown in Fig. 2a. When turning the sound on, particles move toward concentric circles and remain there after the acoustic emission has stopped, as can be seen in Fig. 2b (corresponding Supplementary Movie 1). As also shown, the circles correspond to the pressure antinodes, that stay in the same position as in configuration Fig. 1a since loading negligibly affects the plate modes[14]. This migration is unusual in acoustofluidics regarding the beads acoustic contrast factor which would normally make them move toward the pressure nodes in the Gor'kov framework[17]. Indeed given their density and compressibility ratios, $\tilde{\rho} = \frac{\rho_p}{\rho_l} = 1.05$ and $\tilde{\kappa} = \frac{\kappa_p}{\kappa_l} = 0.72$, respectively, we obtain a positive contrast factor $\Phi = \frac{1}{3}\left(\frac{5\tilde{\rho}-2}{2\tilde{\rho}+1} - \tilde{\kappa}\right) = 0.11 > 0$ (nodal migration particles) in contradiction with the observed antinodal flux. Besides, we observe that larger particles move noticeably faster than smaller ones. In order to quantify this difference, we restrict ourselves to the first Bessel lobe region (center of the plate) to measure the beads radial velocity. Trajectories are extracted from an automated tracking (TrackMate from ImageJ), as presented in Fig. 2c, from which the particle radial velocities are calculated. Thus, for a 1 mm height drop, we measure a maximal velocity of about 300 µm s^{-1} for 100 µm beads to be compared with 10 µm s^{-1} for the 10 µm beads. However, the radial velocity profiles normalized by the maximal value for each particle size are reasonably similar, as shown in Fig. 1d. Interestingly, as also shown in Fig. 2d, with a larger extension displayed on Fig. 2e (blue dots), further decreasing the droplet height to 500 µm yields to a more rapid pattern formation. For this thinner drop, the radial maximal velocity is increased by a factor 6.6, while the pressure raises about a factor 2.4.

Resonance for subwavelength cavity confinment. As suggested by the above mentioned observations, confining the liquid yields to an increased acoustofluidic effect. Hence, having in mind the metamaterial properties of acoustic subwavelength cavities[18] both in terms of sensing[19] or in terms of forces[20], we now confine the liquid within the evanescence length. For that purpose, a hard cover (1-mm-thick glass plate) is placed at a distance h_l in the range 60–890 µm away from the emitter surface. Parallelism is

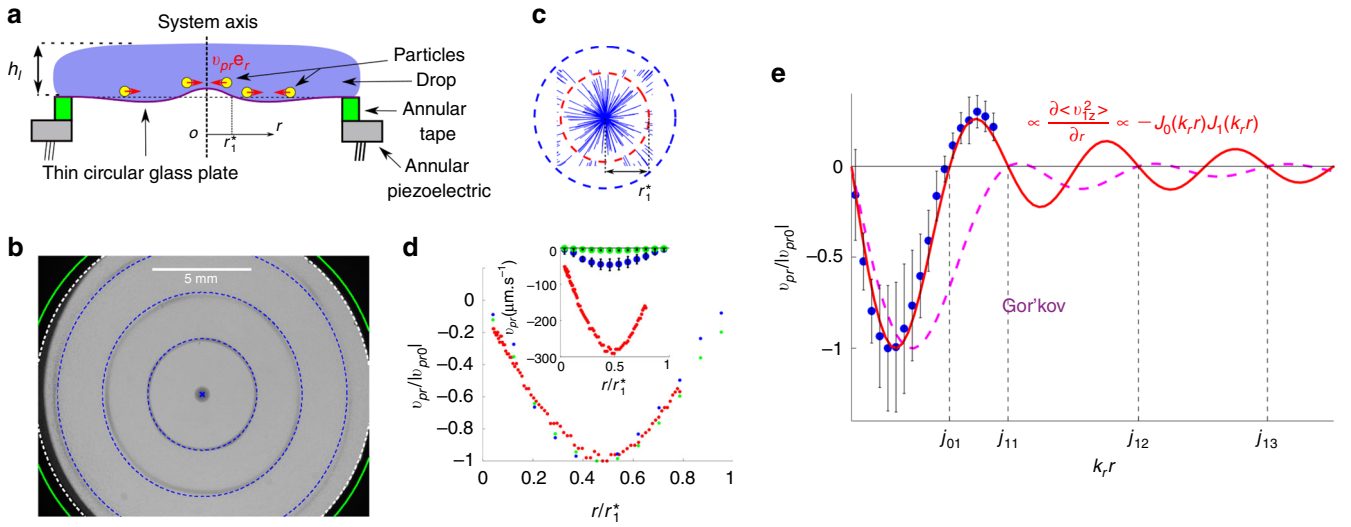

Fig. 2 Microparticle patterning dynamics in an evanescent Bessel beam. **a** Device, with the droplet height denoted h_l. All results are obtained with a voltage $U = 30\ V_{pp}$. **b** Typical ring pattern obtained with $h_l = 500\ \mu m$ and 10 μm microbeads (see Supplementary Movie 1). Blue circles: pressure antinodes; white line: internal border of the piezoceramic; green line: internal border of the annular tape. **c** Tracking of the bead trajectories on the beam axis center, for $h_l = 500\ \mu m$ (see Supplementary Movie 2). The dashed red circle corresponds to the first pressure node, with a radius $r_1^* = 1.7$ mm. The dashed blue circle corresponds to the first pressure antinode out from the plate center. **d** Radial velocity v_{pr} for several bead diameters and drop heights, normalized by the respective maximal value $|v_{pr0}|$, inside the first nodal circle. Red: $h_l = 1$ mm, 100 μm, $v_{pr0} = -284\ \mu m\ s^{-1}$ (single bead). Green: $h_l = 1$ mm, 10 μm, $v_{pr0} = -7\ \mu m\ s^{-1}$ (averaged over 118 beads). Blue: $h_l = 500\ \mu m$, 10 μm, $v_{pr0} = -46\ \mu m\ s^{-1}$ (175 beads). Insert: non normalized curves, error bars giving, as later, the standard deviations. **e** Normalized bead radial velocity as a function of $k_r r$. Blue dots correspond to the experiment Fig. d with the 10 μm beads and $h_l = 500\ \mu m$ (245 beads, bin averages with at least 17 beads per bin). Magenta curve: Gor'kov prediction. Red curve: Velocity prediction assuming a near-field radiation force proportional to $\frac{\partial \langle v_{1z}^2 \rangle}{\partial r}$. j_{mn} is the nth root of the ordinary Bessel function of order m

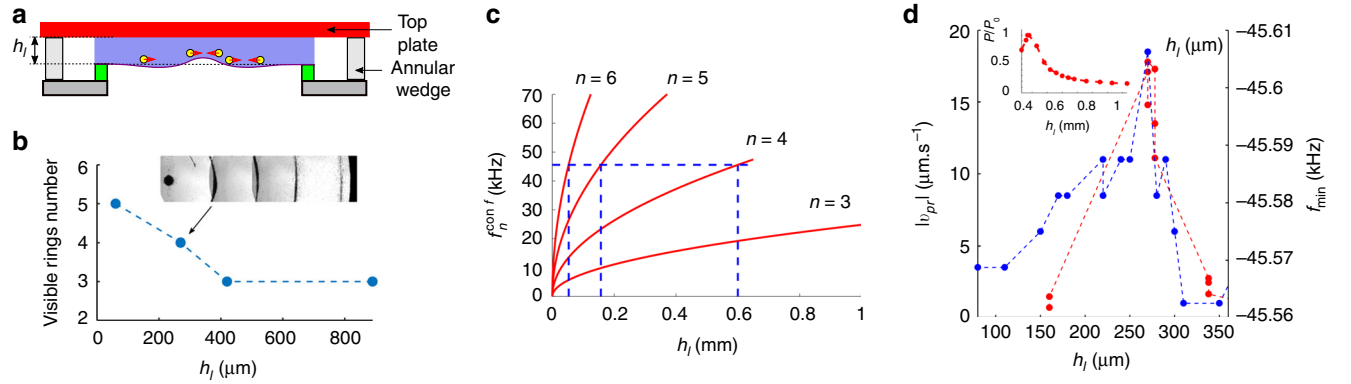

Fig. 3 Enhanced efficiency by subwavelength cavity confinment. **a** Confined device. **b** Number of observed rings as a function of the cavity height h_l. The photograph in insert is a photomontage of three microscope snapshots showing the $n = 4$ mode obtained for $h_l = 270\ \mu m$. **c** Equivalent trilayer system resonant frequencies, as a function of the cavity thickness h_l and number of nodal circles n. The horizontal blue dashed line corresponds to the excitation frequency: a coincidence is obtained for $n \in \{4, 5, 6\}$ at $h_l \in \{600, 157, 53\}\ \mu m$, respectively. **d** Evidence of a resonance for discrete cavity height. Red dots: in terms of radial velocity, with 10 μm polystyrene (PS) beads, for 5 V_{pp}, and 500 μm away from the plate center. Blue dots: in terms of impedance (evolution of the frequency for the device minimal impedance). Insert: in terms of acoustic pressure, with the normalized pressure measured at $z = 130\ \mu m$ normalized by the maximal value of $P_0 = 52$ kPa as a function of the cavity height for $U = 10\ V_{pp}$

ensured by dedicated machined annular polymethylmethacrylate (PMMA) wedges (see Fig. 3a). In the presence of the cover lid, 10 μm PS beads still gather along the same concentric ring structure. However, when reducing h_l, the number of visible rings on the plate increases from 3 to 5 (the outer one being hidden by the piezoelectric). For $h_l > 470\ \mu m$ (i.e. $k_z h_l > 0.6$), the number of rings remains like the non confined case (see Fig. 3b).

The increase in the number of rings when confining liquid can be qualitatively understood by the following reasoning. Given its larger thickness (1 mm), the top plate can be considered as a rigid boundary condition ($D \propto h_s^3$, see Eq. 1), so that the fluid normal velocity vanishes at this surface. Its effect can be estimated by considering an equivalent system, with a doubled liquid height and a top plate identical to the emitting one. This trilayer system with $h_{l,\mathrm{eq}} = 2h_l$ will present no normal motion in the system symmetry plane. For such a system, the plate dynamic writes[21]

$$\rho_l \frac{\partial^2 w}{\partial t^2} = \frac{D h_{l,eq}}{2} \frac{\partial^6 w}{\partial x^6}. \quad (5)$$

Assuming that a resonance occurs when a whole number of wavelength is present on the plate, $n\lambda_f \simeq 2a$ yields to an associated

resonant frequency f_n^{conf} for this confined system

$$f_n^{\mathrm{conf}} = \left(\frac{n}{2a}\right)^3 (2\pi)^2 \left[\frac{Dh_l}{\rho_l}\right]^{\frac{1}{2}}, \quad (6)$$

with $f_n^{\mathrm{conf}}(h_h)$ plotted in Fig. 3c. This simple model thus suggests the existence of discrete peaked resonances when the frequency is set to f_n^{conf}, or equivalently when the height is set to a resonant one, as shown in Fig. 3c for several cavity heights.

Moreover, beads also move faster toward the pressure antinodes for a height close to $h_l = 270\,\mu\mathrm{m}$, about a third of the evanescence length (blue dots in Fig. 3d). In order to verify the existence of an optimal height, two experiments have been conducted. In the first one, we measured the electromechanical impedance of the whole system with reduced heights. In Fig. 3d, the blue dots present the evolution of the resonant frequency (minimal impedance) as a function of the height. Again, an optimal height around $h_l \approx 270\,\mu\mathrm{m}$ is observed. In the second experiment, a dedicated pierced upper plate drilled in its center in order to insert the needle hydrophone has been designed to probe the pressure field in the gap when moving the cover plate (see Supplementary Fig. 3). The insert of Fig. 3d shows that a resonance still occurs since the pressure amplitude presents a peak around $h_l = 370\,\mu\mathrm{m}$. The difference between both values probably stems from the use of a drilled PMMA lid instead of a flat hard one as well as from the intrusiveness of the needle in the near-field.

Migration origin. We now address the issue of the origin of the acoustofluidic force acting on the particle in the near-field region. As noticed earlier (Fig. 2d), the normalized radial velocity of various particles follow the same master curve.

Let us firstly discuss the particle movement in the vicinity of the membrane: do the particles bounce off the plate, roll along it as studied in[22] or do they float in the bulk and are pushed by the acoustic radiation force or streaming flow? For a typical vibration amplitude of the plate estimated to be $A \sim P_0/(\rho_l c_l \omega) = 50\,nm$ (with $P_0 = 20\,\mathrm{kPa}$ extrapolated from Fig. 1c), the particle inertia $\rho_p A\omega^2$ is much larger than its apparent weight $(\rho_p - \rho_l)g$ ($\rho_p A\omega^2/((\rho_p - \rho_l)g) = 10^4 \gg 1$, with ρ_p the particle density and g the gravity acceleration), so that the apparent gravity cannot keep the particles in contact with the plate for a long time. Once in the bulk, particles will settle by gravity (sedimentation) over a time $\tau_g = 9\eta A/[2r_p^2(\rho_p - \rho_l)g]$. Since τ_g is much larger that the acoustic period $2\pi/\omega$, the particle won't have time to settle down provided that the acoustic amplitude is large enough so that second-order acoustic effects come into play. Consequently they will eventually be either captured and dragged by the acoustic streaming flow, or pushed by the acoustic radiation force.

As for the streaming, the typical streaming velocity scales like $(A\omega)^2/c_s = 1\,\mu\mathrm{m\,s}^{[-1}$[23]. This streaming velocity becomes comparable with the particle velocity when using tiny particles as small as 500 nm diameter fluorescent tracers (Supplementary Movie 3) for which we measured a maximal velocity of $2\,\mu\mathrm{m\,s}^{-1}$ in a 1-mm drop. Nevertheless, both 10 μm and 100 μm particles move much faster ($7\,\mu\mathrm{m\,s}^{-1}$ and $284\,\mu\mathrm{m\,s}^{-1}$, respectively, see Supplementary Fig. 4). The observed difference in magnitude discards a streaming-dominated migration and suggests a radiation force mechanism.

For a subwavelength particle of radius $r_p \ll \lambda_l$ (Rayleigh diffusion regime) in an infinite medium, the radiation force is given by the celebrated Gor'kov formula: $\mathbf{F}_{\mathrm{rad},G} = -\nabla U_{\mathrm{rad}}$, with $U_{\mathrm{rad}} = V_p\left[\frac{f_1}{2}\kappa_l\langle p_1^2\rangle - \frac{3}{4}f_2\rho_l\langle \mathbf{v}_1^2\rangle\right]$, $f_1 = 1 - \tilde{\kappa}$ and $f_2 = 2(\tilde{\rho}-1)/(1+2\tilde{\rho})$, V_p being the particle volume[17,24]. Here, the acoustic velocity $\boldsymbol{v}_1$ is first derived from the linearized Euler equation knowing the pressure field p_1 (Eq. 4), leading to $\boldsymbol{v}_1 = \frac{p_0}{\rho_l\omega}(k_r J_1(k_r r)\boldsymbol{e}_r + k_z J_0(k_r r)\boldsymbol{e}_z)e^{-k_z z}\sin(\omega t)$. Assuming this force is balanced by a viscous drag $\mathbf{F}_s \propto 6\pi\eta_l r_p(\mathbf{v}_p - \mathbf{v}_2)$[25] ($\mathbf{v}_2$: streaming), the resulting velocity profile $v_p(r)$ is presented in Fig. 2e (magenta curve). Here, the Gor'kov approach clearly fails to predict the radiation force. Unfortunately to date, no near-field expression for the radiation force exists. Using a phenomenological approach, we searched for a corrected expression that is proportional to one of the three second-order acoustofluidic terms $-\frac{\partial\langle p_1^2\rangle}{\partial r}$, $\frac{\partial\langle v_{1r}^2\rangle}{\partial r}$, and $\frac{\partial\langle v_{1z}^2\rangle}{\partial r}$. As shown in Fig. 2e, the term $\frac{\partial\langle v_{1z}^2\rangle}{\partial r} \propto \frac{\partial J_0(k_r r)^2}{\partial r}$ predicts very well the measured evolution, as opposed to the two other terms (see details in Supplementary Fig. 5). A more detailed analysis of the radial scaling of the streaming also allows to conclude that the migration of the 10-μm beads in the 500 μm drop originates from the near-field radiation force, as shown in Supplementary Figs 6 and 7. The increase of velocity by a factor of 6.6 when h_l is decreased from 1 mm to 500 μm is also in accordance with its quadratic dependence on the pressure, which increases by a factor 2.4 ($2.4^2 = 6$).

In the Supplementary Note 1, we briefly present two key-application of the sub-wavelength confined device. In particular, we show that by thinning the glass substrate down to 30 μm, higher resonant frequencies can be achieved in order to increase the radiation force magnitude. Thus, living organisms as small as bacteria can be patterned along concentric circles thanks to the enhanced radiation force arising from the evanescent field. In addition, we also present a more surprising capability of plasma extraction when dealing with whole blood from patients (see also Methods). These stimulating results are let for future dedicated research.

Use of a trapped resonant bubble. Microbubbles are widely used in microfluidics since they act as a local amplifier of the forcing acoustic field. As they respond to low-frequency, they are in general excited by low-frequency bulk waves[26,27]. In this section, we present the interest of using a bubble trapped in the axis of the Bessel evanescent field. Indeed, the well-known streaming capability of excited microbubble here competes with the strong inward radiation force associated with the Bessel field on which the bubble is trapped.

Gas bubbles of initial radius around $r_b > 25\,\mu\mathrm{m}$ are created by water electrolysis using a pair of electrodes, one of them being placed just on top of the plate center, when sound is present. Alignment with a mark on the bottom plate is ensured by means of a microscope. As a result of the acoustic field, the bubbles are attracted to the bottom emitting plate, where they remain anchored even after having switched the sound off. The resulting "pendent" bubble holds to the bottom glass by capillarity[26] with a contact angle of about 20°.

When sound is present, bubbles grow with time by rectified diffusion[28] allowing us to slowly vary the bubble radius up to 110 μm, keeping the forcing frequency $f = 45\,kHz$ constant. The surrounding liquid is seeded with microparticles of radius r_p from 1 μm to 40 μm. A high speed imaging system is mounted on the microscope in order to image the fast bubble dynamics (see Methods).

At a low acoustic amplitudes, the bubble oscillates radially (breathing mode) for a large range of radius (typically [30–110]μm). A maximum response is obtained around $r_b = 50\,\mu\mathrm{m}$. When the acoustic amplitude is further increased, we observe the trigger of a parametric instability (Supplementary Movie 4 and Supplementary Figs. 8 and 9) as already reported for both tethered, free bubbles and confined flat bubbles[29–31]. In this

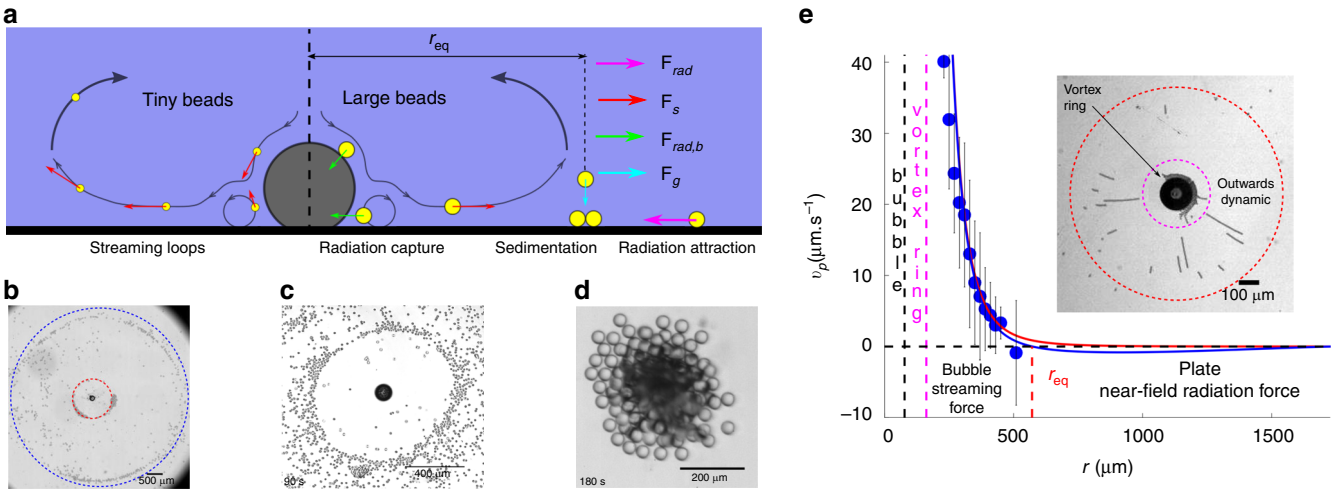

Fig. 4 Microparticle repulsion and capture by addition of a trapped resonant bubble. **a** Illustration of the typical dynamics of tiny and large beads around a pulsating bubble located on the Bessel beam axis. The main forces are represented: $\mathbf{F}_{\mathrm{rad}}$ the near-field radiation force, $\mathbf{F}_s$ the bubble-induced streaming force, $\mathbf{F}_{\mathrm{rad},b}$ the secondary radiation force arising from the bubble pulsation and $\mathbf{F}_g$ the buoyancy force. **b** 40 µm beads repelled by a 85 µm radius bubble collecting around the red circle of radius $r_{\mathrm{eq}} = 609$ µm. The Bessel ring (for an infinite loading) corresponds to the blue circle. Voltage of 5 V_{pp} and $h_l =$ 470 µm. **c** Repulsion of HeLa cells with a 55 µm radius bubble ($h_l = 500$ µm, $U = 5$ V_{pp}). **d** Capture of 40 µm polystyrene spheres with a 29 µm radius bubble ($h_l = 120$ µm, $U = 5$ V_{pp}). **e** 5 µm bead velocities around a $r_b = 78$ µm bubble. Voltage of 7 V_{pp} and $h_l = 500$ µm. Blue dots: mean velocities from 12 beads tracking, within 20 µm wide bins. Error bars display the standard deviations. Red curve: theoretical streaming $v_s = v_{s0}\left(\frac{r_0}{r}\right)^5$, where $r_0 = 300$ µm and v_{s0} is the measured velocity at r_0 ($v_s(r_0) = 19$ µm s^{-1}). Blue curve: bead velocity obtained from the cumulative effects of the bubble microstreaming force (red curve) and the near-field plate radiation force. An equilibrium is obtained for $r = r_{\mathrm{eq}}$. Insert: overlay of minimal intensities over 10 s in the present experiment. Beads move outwards between the magenta and red circles ($162 < r < 510$ µm), and join an inner vortex ring for lower radii positions. The bubble pulsation amplitude is 4 µm

regime, the streaming is expected to be stronger[32] and subharmonic surface waves propagate along the bubble interface, superimposed on the breathing mode. Overall, in the presence of particles, various patterns are observed going from more or less complex streaming loops (see Fig. 4a, left side) to bubble repulsion (Fig. 4b, c) or attraction (Fig. 4d) depending on the particle size, bubble diameter, confinement and applied voltage (see Supplementary Movies 5–9 for several examples).

Discussion

Classically, a free bubble resonant frequency can be estimated by $f_{b0} = \frac{1}{2\pi r_b}\sqrt{\frac{3\gamma p_0}{\rho_l}}$ [28] (γ: adiabatic index, p_0: static pressure). The confinement lowers the resonant frequency and broadens the bubble response (decrease of the quality factor). The present contact angle of 20° predicts a modified eigenfrequency $f_{b0c} = 0.83 f_{b0}$[33], or equivalently a resonant radius of 60 µm, in reasonable agreement with our measurements.

The microstreaming from an axisymmetrically pulsating pendent bubble has been calculated by Elder[34] and is qualitatively sketched in Fig. 4a. Let us now try to give an interpretation of the observed behaviors by following this figure. In the absence of bubble, particles migrate radially inward (toward the Bessel beam axis), pushed by the above-studied near-field radiation force F_{rad}. When a bubble is added, the induced outer streaming near the plate is directed outwards (see Fig. 4a, right side) so that both effects compete. Therefore, beads are likely to gather at a certain distance r_{eq} away from the bubble center where both force F_s and F_{rad} balance. Indeed, as shown in Fig. 4b an additional ring at $r = r_{\mathrm{eq}}$ away from the bubble is formed on top of the original and larger Bessel ring stemming from the plate mode (see also Supplementary Movie 6). Depending on their buoyancy (force F_g in Fig. 4a), particles can either turn in the loops of the outer streaming (see Fig. 4a and Supplementary Movie 7 for 1 µm particles) or migrate to finally settle at $r = r_{\mathrm{eq}}$ so that a clear depleted region appears between $r = r_b$ and r_{eq} (see Fig. 4c for an example with HeLa cells). Let us estimate r_{eq}: at the plate level, the bubble-induced outer streaming $\boldsymbol{v}_s$ can be estimated by $v_s = \frac{\xi\omega r_b^7}{r^5}$ [34]. This estimate is in fairly good agreement with the tracking of 5 µm beads (see red curve in Fig. 4e and Supplementary Movie 10), except near and far from the bubble. Taking the inward near-field radiation force F_{rad} into account, which is proportional to $-P_0^2\frac{\partial J_0^2}{\partial r^2}$, leads to a bead velocity $v_p = -\alpha P_0^2\frac{\partial J_0^2}{\partial r^2}$, where α depends on the particle radius. Figure 4e (blue curve) shows the radial velocity resulting from both contributions (see also Supplementary Fig. 10 and Supplementary Movie 11). As expected, the contribution of the radiation force is small in comparison with the streaming force but both balance at $r_{\mathrm{eq}} =$ 537 µm (horizontal velocity cancellation) close to the observed ring in Fig. 4e.

Now, when the plate inward radiation force F_{rad} dominates the outer streaming force F_s particles are attracted towards the beam axis matching the bubble location. When approaching the bubble wall, particles will eventually be captured by the short-range secondary radiation force $F_{\mathrm{rad},b}$ emanating from the pulsating bubble, as recently reported[27]. The attraction effect is maximized when the device is confined (so that the near-field radiation force is enhanced) and when the streaming is weak (for a non resonating bubble) - see Supplementary Movie 10 and Fig. 4d. In addition, as the capture mechanism depends on the combination of two radiation forces F_{rad} and $F_{\mathrm{rad},b}$ (which both scale like r_p^3) this regime is observed only for large enough particles (>40 µm) for which the streaming contribution is vanishingly small ($F_s \sim r_p$).

Finally, for the case of tiny particles ($r_p < 5$ µm), and provided that the bubble pulsation is strong enough, the near-field radiation force is in general too weak to compete with the streaming so that more classic continuous streaming loops are observed (both inner and outer) around the bubble (left side of Fig. 4a).

To summarize, the stable trapping of a microbubble in the Bessel beam axis enabled us to reverse the central plate pattern

and use bubbles as acoustic magnet for attracting, repelling or mixing the surrounding particles.

We have demonstrated the possibility of creating an evanescent acoustic Bessel beam of order zero by low-frequency ultrasound. Interestingly, the subsonic regime of plate wave propagation results in the generation of unusually strong spatial gradients. Consequently, we have succeeded in arranging either microbeads, HeLa cells and bacteria in concentric ring patterns that correspond to the antinodes of the pressure Bessel field. As we have shown, particles are pushed by the strong near-field radiation force, whose expression differs from the conventional bulk one due to the evanescence of the field. When the beam is confined to a sub-wavelength cavity, the Bessel beam radial wavelength is decreased, enhancing the force and leading to some height dependent resonances. This field enhancement is very close to the one evidenced for slotted phononic crystal plates, arranged in a subwavelength cavity mode[18,20] with periodically grooved structures.

As recently shown in plasmonics, the confinement of optical vortices[35] or of evanescent vortex Bessel beam[36] is a promising approach to achieve powerful optical spanners. Likewise, we believe that adding an azimuthal phase control of the excitation will generate higher order evanescent acoustic Bessel beam and acoustic vortices. This strategy, recently demonstrated for acoustorotation in the case of evanescent plane waves[7], opens the route toward flexible trapping and spinning of individual living cells in culture conditions. Overall, we believe that extending acoustic manipulation to the near-field domain will open unprecedented opportunities to fill the gap between conventional (propagative) acoustofluidics and the recent rise of phononics and acoustic metamaterials.

Methods

Device fabrication. The piezoelectric has a 4-mm-thick ring shape, with a 17–33-mm internal and external diameters (NCE80, Noliac). The circular glass coverslip has a 20 mm diameter (Menzel-Gläser). The fixing double sided tape is cut to a ring shape of internal radius 9 mm with a cutting machine Craft Robo (Graphtec). Two contacts are made by fixing electric wires with silver conductive paint, and the resonance is measured with a spectrum analyzer (4195A, Hewlett Packard). For the unconfined study, the plastic cylinder is a section of a 50 mL Falcon.

Pressure measurements. The pressure measurements are performed using an hydrophone from Precision Acoustics, with a needle of 1.5 mm outer diameter, holding a 1 mm diameter polyvinylidene fluoride (PVDF) membrane.

Imaging. The device is mounted on the microscope with a home made aluminum and PMMA support (see Supplementary Fig. 3). The sub-periodic bubble dynamics are resolved with a high speed camera (Fastcam SA1.1, Photron) mounted on an inverted microscope (Eclipse, Nikon). Supplementary Movie 12 is obtained with a ×6 (×4 × 1.5) magnification and Hg illumination. The bacteria patterns are imaged with a large field camera (ORCA-flash4.0, Hamamatsu) mounted on a reflected-light microscope (Zeiss Axioplan II) equipped for fluorescent imaging and a 5× objective.

Microparticles. All polystyrene microparticles are purchased from Fluka, with the indicated sizes referring to the particle diameter.

Blood samples. Whole human blood samples were obtained from healthy donors (Établissement Français du Sang (EFS), Grenoble, France) and were collected in citrate vacutainer tubes (Becton Dickinson, Le Pont de Claix, France). Samples were used without any dilution and the blood tubes were delivered three days after withdrawal and were kept at 4 °C in a fridge for storage. The experiments were performed within three days after delivery.

Ethics statement. Experiments with blood are performed according to the ethical and legal standards of our blood supplier (EFS). Informed consent was given by blood donors.

Reporting summary. Further information on research design is available in the Nature Research Reporting Summary linked to this article.

Data Availability

The data that support the findings of this study are available from the corresponding author upon reasonable request.

Received: 7 January 2019 Accepted: 11 July 2019
Published online: 05 September 2019

References

1. Ashkin, A., Dziedzic, J. M., Bjorkholm, J. & Chu, S. Observation of a single-beam gradient force optical trap for dielectric particles. *Opt. Lett.* **11**, 288–290 (1986).
2. Salomon, C., Dalibard, J., Aspect, A., Metcalf, H. & Cohen-Tannoudji, C. Channeling atoms in a laser standing wave. *Phys. Rev. Lett.* **59**, 1659 (1987).
3. Juan, M. L., Righini, M. & Quidant, R. Plasmon nano-optical tweezers. *Nat. Photon.* **5**, 349 (2011).
4. Volpe, G., Quidant, R., Badenes, G. & Petrov, D. Surface plasmon radiation forces. *Phys. Rev. Lett.* **96**, 238101 (2006).
5. Friend, J. & Yeo, L. Y. Microscale acoustofluidics: microfluidics driven via acoustics and ultrasonics. *Rev. Mod. Phys.* **83**, 647–704 (2011).
6. Black, J. P., White, R. M. & Grate, J. W. Microsphere capture and perfusion in microchannels using flexural plate wave structures. *IEEE Int. Ultrason. Symp.* **1**, 475–479 (2002).
7. Aubert, V. et al. A simple acoustofluidic chip for microscale manipulation using evanescent Scholte waves. *Lab Chip* **16**, 2532–2539 (2016).
8. Vuillermet, G., Gires, P.-Y., Casset, F. & Poulain, C. Chladni patterns in a liquid at microscale. *Phys. Rev. Lett.* **116**, 184501 (2016).
9. Durnin, J., Miceli, J. Jr & Eberly, J. Diffraction-free beams. *Phys. Rev. Lett.* **58**, 1499 (1987).
10. Imani, M. F. & Grbic, A. Generating evanescent Bessel beams using near-field plates. *IEEE Trans. Antennas Propag.* **60**, 3155–3164 (2012).
11. Courtney, C. R. et al. Dexterous manipulation of microparticles using Bessel-function acoustic pressure fields. *Appl. Phys. Lett.* **102**, 123508 (2013).
12. Baresch, D., Thomas, J.-L. & Marchiano, R. Spherical vortex beams of high radial degree for enhanced single-beam tweezers. *J. Appl. Phys.* **113**, 184901 (2013).
13. Baresch, D., Thomas, J.-L. & Marchiano, R. Observation of a single-beam gradient force acoustical trap for elastic particles: acoustical tweezers. *Phys. Rev. Lett.* **116**, 024301 (2016).
14. Amabili, M. & Kwak, M. Free vibrations of circular plates coupled with liquids: revising the Lamb problem. *J. Fluids Struct.* **10**, 743–761 (1996).
15. Kinsler, L. E., Frey, A. R., Coppens, A. B. & Sanders, J. V. *Fundamentals of Acoustics* (Wiley: New York, 2000).
16. Morse, P. & Ingard, K. *Theoretical Acoustics* (Princeton University Press, Princeton, 1986).
17. Bruus, H. Acoustofluidics 7: the acoustic radiation force on small particles. *Lab Chip* **12**, 1014–1021 (2012).
18. Cai, F., Li, F., Meng, L., Wu, J. & Zheng, H. Strong localization of an acoustic wave in a sub-wavelength slot between two plates. *J. Acoust. Soc. Am.* **137**, 1251–1256 (2015).
19. Qiu, C., Xu, S., Ke, M. & Liu, Z. Acoustically induced strong interaction between two periodically patterned elastic plates. *Phys. Rev. B* **90**, 094109 (2014).
20. Wang, C. et al. A highly sensitive compact liquid sensor based on slotted phononic crystal plates. *Lab Chip* **16**, 4595–4600 (2016).
21. Hassan, W. & Nagy, P. On the low-frequency oscillation of a fluid layer between two elastic plates. *J. Acoust. Soc. Am.* **102**, 3343–3348 (1997).
22. Van Gerner, H. J., van der Hoef, M. A., Van Der Meer, D. & Van Der Weele, K. Inversion of Chladni patterns by tuning the vibrational acceleration. *Phys. Rev. E* **82**, 012301 (2010).
23. Rayleigh, L. On the circulation of air observed in Kundt's tubes, and on some allied acoustical problems. *Philos. Trans. R. Soc. Lond.* **175**, 1–21 (1884).
24. Gor'kov, L. On the forces acting on a small particle in an acoustical field in an ideal fluid. *Sov. Phys. -Dokl.* **6**, 773–775 (1962).
25. Happel, J. & Brenner, H. *Low Reynolds Number Hydrodynamics: With Special Applications to Particulate Media*. (Martinuis Nijhoff, The Hague, 1983).
26. Tho, P., Manasseh, R. & Ooi, A. Cavitation microstreaming patterns in single and multiple bubble systems. *J. Fluid Mech.* **576**, 191–233 (2007).
27. Rogers, P. & Neild, A. Selective particle trapping using an oscillating microbubble. *Lab Chip* **11**, 3710–3715 (2011).
28. Leighton, T. *The Acoustic Bubble*. (Academic Press, Cambridge, 1994).
29. Maksimov, A. O., Leighton, T. G. & Birkin, P. R. Self focusing of acoustically excited Faraday ripples on a bubble wall. *Phys. Lett. A* **372**, 3210–3216 (2008).
30. Dangla, R. & Poulain, C. When sound slows down bubbles. *Phys. Fluids* **22**, 041703 (2010).
31. Mekki-Berrada, F., Thibault, P. & Marmottant, P. Acoustic pulsation of a microbubble confined between elastic walls. *Phys. Fluids* **28**, 032004 (2016).
32. Maksimov, A. Viscous streaming from surface waves on the wall of acoustically-driven gas bubbles. *Eur. J. Mech. B/Fluids* **26**, 28–42 (2007).

33. Maksimov, A. On the volume oscillations of a tethered bubble. *J. Sound Vib.* **283**, 915–926 (2005).
34. Elder, S. A. Cavitation microstreaming. *J. Acoust. Soc. Am.* **31**, 54–64 (1959).
35. Mei, S. et al. Evanescent vortex: optical subwavelength spanner. *Appl. Phys. Lett.* **109**, 191107 (2016).
36. Rui, G., Wang, X. & Cui, Y. Manipulation of metallic nanoparticle with evanescent vortex Bessel beam. *Opt. Express* **23**, 25707–25716 (2015).

Acknowledgements

This work was supported by recurrent funding from the Commissariat à l'Énergie Atomique et aux Énergies Alternatives (CEA) and specific fundings through the CARNOT program (LETI institute, ABCDE grant). Authors wish to thank Lee Bernick (MIT-Giant exchange student program) for the bacteria experiments and Pierre Marcoux (LETI-CEA) for the fluorescent *E. coli* cultures.

Author contributions

C.P. proposed and supervised the project. P.-Y.G. performed the experiments and analyzed the data. Both authors wrote and commented on the manuscript.

Additional information

Supplementary information accompanies this paper at https://doi.org/10.1038/s42005-019-0191-z.

Competing interests: The authors declare no competing interests.

Reprints and permission information is available online at http://npg.nature.com/reprintsandpermissions/

Publisher's note: Springer Nature remains neutral with regard to jurisdictional claims in published maps and institutional affiliations.